

Structure- and function-based design of *Plasmodium*-selective proteasome inhibitors

Hao Li^{1,2†}, Anthony J. O'Donoghue^{3†}, Wouter A. van der Linden¹, Stanley C. Xie⁴, Euna Yoo², Ian T. Foe², Leann Tilley⁴, Charles S. Craik³, Paula C. A. da Fonseca⁵ & Matthew Bogoy²

The proteasome is a multi-component protease complex responsible for regulating key processes such as the cell cycle and antigen presentation¹. Compounds that target the proteasome are potentially valuable tools for the treatment of pathogens that depend on proteasome function for survival and replication. In particular, proteasome inhibitors have been shown to be toxic for the malaria parasite *Plasmodium falciparum* at all stages of its life cycle^{2–5}. Most compounds that have been tested against the parasite also inhibit the mammalian proteasome, resulting in toxicity that precludes their use as therapeutic agents^{2,6}. Therefore, better definition of the substrate specificity and structural properties of the *Plasmodium* proteasome could enable the development of compounds with sufficient selectivity to allow their use as anti-malarial agents. To accomplish this goal, here we use a substrate profiling method to uncover differences in the specificities of the human and *P. falciparum* proteasome. We design inhibitors based on amino-acid preferences specific to the parasite proteasome, and find that they preferentially inhibit the $\beta 2$ -subunit. We determine the structure of the *P. falciparum* 20S proteasome bound to the inhibitor using cryo-electron microscopy and single-particle analysis, to a resolution of 3.6 Å. These data reveal the unusually open *P. falciparum* $\beta 2$ active site and provide valuable information about active-site architecture that can be used to further refine inhibitor design. Furthermore, consistent with the recent finding that the proteasome is important for stress pathways associated with resistance of artemisinin family anti-malarials^{7,8}, we observe growth inhibition synergism with low doses of this $\beta 2$ -selective inhibitor in artemisinin-sensitive and -resistant parasites. Finally, we demonstrate that a parasite-selective inhibitor could be used to attenuate parasite growth *in vivo* without appreciable toxicity to the host. Thus, the *Plasmodium* proteasome is a chemically tractable target that could be exploited by next-generation anti-malarial agents.

The *Plasmodium* proteasome represents a viable target for anti-malarial drugs owing to its essential nature in protein turnover and the parasite's need to rapidly divide inside host cells⁹. We have previously shown that differences exist in the reliance of human cells and *P. falciparum* on specific proteasome activities for survival¹⁰. Therefore, we reasoned that a structural and biochemical understanding of this enzyme complex could yield compounds with desirable safety profiles due to their selectivity for the parasite proteasome. We purified the *P. falciparum* 20S proteasome¹¹, activated it with human PA28 α ^{12,13} (Extended Data Fig. 1a), and determined the substrate preferences of this activated proteasome by monitoring the degradation pattern of 228 diverse synthetic tetradecapeptides using liquid chromatography–tandem mass spectrometry^{14,15}. A frequency profile was generated using iceLogo software¹⁶, indicating which amino acids were most and

least favoured in the subsites surrounding each cleaved bond. In parallel, we generated a substrate specificity profile for the human 20S/PA28 α proteasome under identical conditions. We detected 284 and 328 cleavage sites for the activated *P. falciparum* and human 20S proteasomes, respectively, with 171 sites being cleaved by both (Fig. 1a). However, 113 and 157 sites were uniquely cleaved by *P. falciparum* and human proteasomes, respectively (Fig. 1a–c and Extended Data Fig. 1b, c), with the major differences occurring on the amino (N)-terminal side of the cleavage site, namely at the P1 and P3 sites. For the P1 position which is directly adjacent to the cleavage site, the human proteasome showed chymotrypsin-like (Leu/Phe/Tyr), trypsin-like (Arg), and caspase-like (Asp) activity (Fig. 1b), consistent with previous studies¹⁷, while the *P. falciparum* proteasome showed strong preference for aromatic residues (Fig. 1c). Direct comparison of the specificity profiles of both proteasomes revealed a clear preference for Trp at P1 and P3 in the parasite proteasome (Fig. 1d and Extended Data Fig. 1b, c).

Using the canonical tri-leucine scaffold found in common proteasome inhibitors such as MG132 and Z-L3-VS^{18,19}, we systematically replaced the Leu residues at the P1 and P3 positions with Trp, resulting in the compounds LLW-vs, WLL-vs and WLW-vs (Fig. 1e and Extended Data Fig. 2a). We treated purified *P. falciparum* 20S proteasomes with each compound and measured residual activity of the catalytic sites using an activity-based probe¹⁰ (Fig. 1f). Changing the P1 position to Trp (LLW-vs) markedly reduced inhibition of the $\beta 5$ active site, without altering the activity towards the $\beta 2$ -subunit, while Trp in the P3 position (WLL-vs) resulted in potent inhibition of both $\beta 2$ and $\beta 5$ activities. Finally, Trp substitution in both P1 and P3 positions (WLW-vs) resulted in a potent inhibitor that was highly selective for the parasite proteasome $\beta 2$ -subunit. With the exception of LLW-vs, these compounds inhibited the human $\beta 5$ -subunit while all compounds only weakly inhibited the human $\beta 1$ and $\beta 2$ activities (Fig. 1g and Extended Data Figs 1d and 2b). Therefore, these inhibitors primarily differ in their selectivity towards the $\beta 2$ -subunits and this selectivity was retained in human and *P. falciparum* inhibitor treatments in live culture (Extended Data Fig. 2c).

We investigated the structural basis for the $\beta 2$ selectivity of the *P. falciparum* 20S proteasome towards WLW-vs by high-resolution cryo-electron microscopy (cryo-EM) and single-particle analysis, using a strategy similar to that which we previously used to determine the structure of an inhibitor-bound human 20S proteasome²⁰. The resolution of the final map was estimated at 3.6 Å (Fig. 2 and Extended Data Fig. 3a–e), with local resolution decreasing for solvent exposed surfaces (Fig. 2a, b). In our map, sheet-forming β -strands are well resolved (Fig. 2d) and side chains are well defined for both β -strands and α -helices (Fig. 2e, f), particularly when stabilized by intra-protein contacts or steric restraints. We were able to unambiguously assign a

¹Department of Chemical and Systems Biology, Stanford University School of Medicine, Stanford, California 94305, USA. ²Department of Pathology, Stanford University School of Medicine, Stanford, California 94305, USA. ³Department of Pharmaceutical Chemistry, University of California San Francisco, San Francisco, California 94158, USA. ⁴Department of Biochemistry and Molecular Biology, Bio21 Institute, University of Melbourne, Melbourne 3010, Victoria, Australia. ⁵MRC Laboratory of Molecular Biology, Francis Crick Avenue, Cambridge Biomedical Campus, Cambridge CB2 0QH, UK. [†]Present addresses: Molecular Engineering Laboratory, Biomedical Sciences Institute, Agency for Science, Technology and Research, Singapore 138673 (H.L.); Skaggs School of Pharmacy and Pharmaceutical Sciences, University of California San Diego, La Jolla, California 92093, USA (A.J.O.).

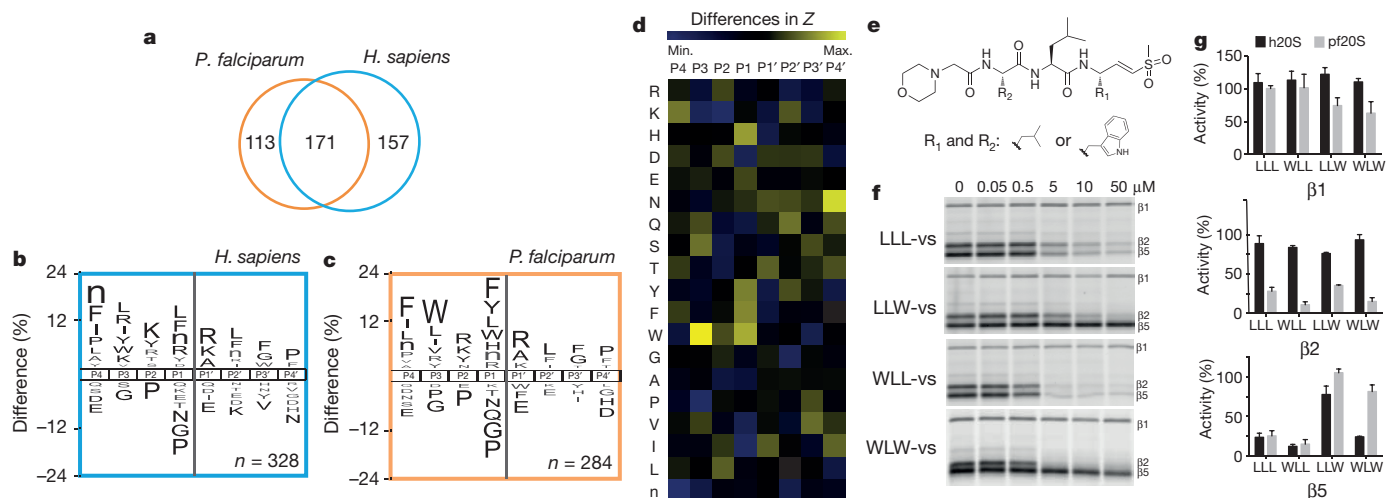


Figure 1 | Substrate profile of the activated human and *P. falciparum* 20S proteasome guides inhibitor design. **a**, Total number of cleavage sites detected after incubation for 4 h of the activated human and *P. falciparum* proteasome with the peptide library. **b**, **c**, The iceLogos generated from the cleavages are shown for human (**b**) and *P. falciparum* (**c**) proteasome. Amino acids that are most and least favoured at each position are shown above and below the axis, respectively. Lower-case 'n', norleucine; amino acids in black text are statistically significant ($P < 0.05$, unpaired two-tailed Student's *t*-test). **d**, The Z-score for amino acids at each position (P4–P4') was calculated for both the human and the parasite proteasome on the basis of the cleavages in **a**, and the difference between the Z-scores

is shown as a heatmap. **e**, Inhibitors are designed by substituting Trp at either the P1 and/or P3 positions in the morpholino-capped tri-leucine vinyl sulfone. Residue 1 (R_1) and 2 (R_2) refer to the amino acids Leu or Trp. **f**, Inhibition of purified *P. falciparum* 20S as assessed by activity-based probe labelling. The same experiment was repeated for the human 20S proteasome (Extended Data Fig. 2b). **g**, Activity of each subunit in human or *P. falciparum* proteasome after 10 μ M inhibitor treatment was determined by image quantification of the intensity of probe labelling and normalized to mock-treated control. Error bars, s.d. $n = 3$ purified proteasome from three independent experiments (for gel source data, see Supplementary Fig. 1a, b).

clear density extending from the $\beta 2$ -subunit N-terminal threonine to the WLW-vs inhibitor, with the vinyl sulfone group and the WLW side chains clearly resolved in a β -strand secondary structural conformation (Fig. 2g).

When the protein coordinates for the *P. falciparum* $\beta 1$ - and $\beta 5$ -subunits are aligned to those of the ligand-bound $\beta 2$ -subunit, the resulting superimposition of the WLW-vs ligand into the $\beta 1$ and $\beta 5$ active sites clearly reveals space constraints for its binding. While the more open conformation of the $\beta 2$ binding pocket easily accommodates the WLW-vs side chains (Fig. 3a), the ligand overlay into the $\beta 1$ and $\beta 5$ active sites results in the burying of its Trp side chains into the protein van der Waals surface (Fig. 3b, c), with the exception of the P3 position in the $\beta 5$ active site (Fig. 3c). We extended this comparison to the protein coordinates of the human 20S proteasome active sites, using the coordinates of the human apo complex²¹ (Protein Data Bank (PDB) accession 4R3O). Superimposing the WLW-vs inhibitor onto the human apo proteasome core (Fig. 3d–f) shows its active sites have no accessibility for the P1 and P3 Trp side chains of the inhibitor, with the exception of the P3 position at the $\beta 5$ active site (Fig. 3f). Similar observations can be made when using the protein model of the human proteasome core bound to the inhibitor AdaAhx₃-LLL-vs (PDB 5A0Q) (Extended Data Fig. 3f–h). This structural comparison of the accessibility of *P. falciparum* and human proteasome active sites is consistent and explains the observed specificity of the WLW-vs inhibitor towards the *P. falciparum* $\beta 2$ -subunit, which would be difficult to predict without direct high-resolution structural information. The results presented here show an important and novel application of high-resolution cryo-EM to interpret the basis for the specific binding of a ligand to an active site, where the information obtained can be harnessed to guide further ligand development for therapeutic usage.

P. falciparum parasites can become resistant to killing by the front-line artemisinin (ART) drug family^{22–24}; however, these ART-treated parasites are particularly sensitive to disruption of normal proteasome function²⁵. We previously showed that inhibition of the proteasome $\beta 5$ -subunit is required for attenuation of *P. falciparum* growth¹⁰. However, we reasoned that a sublethal dose of the *Plasmodium*

$\beta 2$ -selective inhibitor WLW-vs may still be sufficient to enhance killing by ART in both sensitive and resistant parasites. When laboratory-adapted clinical isolates were treated at the early ring stage of the intraerythrocytic cycle, ART-resistant parasites (PL7) showed close to twofold higher sensitivity to WLW-vs than ART-sensitive parasites (PL2) (Fig. 4a). In addition, we observed synergism between dihydroartemisinin (DHA) and WLW-vs at concentrations where WLW-vs selectively inhibits the $\beta 2$ -subunit of the *Plasmodium* proteasome (Fig. 4b and

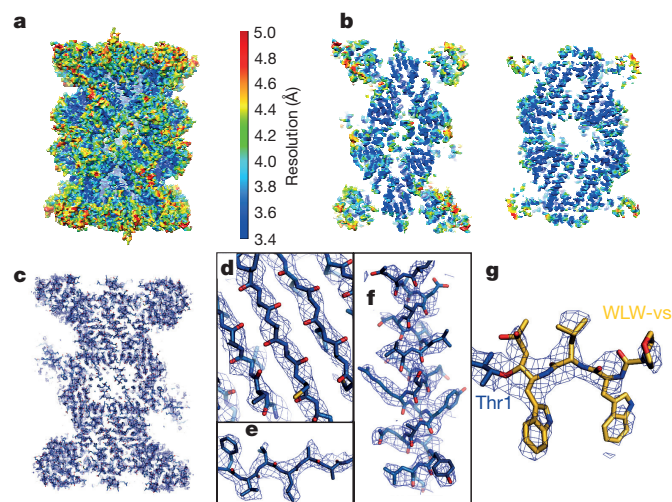


Figure 2 | Structure of the *P. falciparum* 20S proteasome core bound to the inhibitor WLW-vs, determined by cryo-EM and single-particle analysis. **a**, The cryo-EM map is surface rendered and colour coded according to local resolution as determined by ResMap. **b**, Sections of the map as shown in **a**, revealing the higher resolution at the internal regions of the complex, compared with solvent exposed surfaces. **c**, Section of the cryo-EM map, as mesh representation, showing the overall fitting of the protein model. **d**–**g**, Detailed views of the map showing clear separation of sheet-forming β -strands (**d**), good recovery of side chains, both in β -strands (**e**) and α -helices (**f**), and the densities for the WLW-vs inhibitor at the proteasome $\beta 2$ active site (**g**).

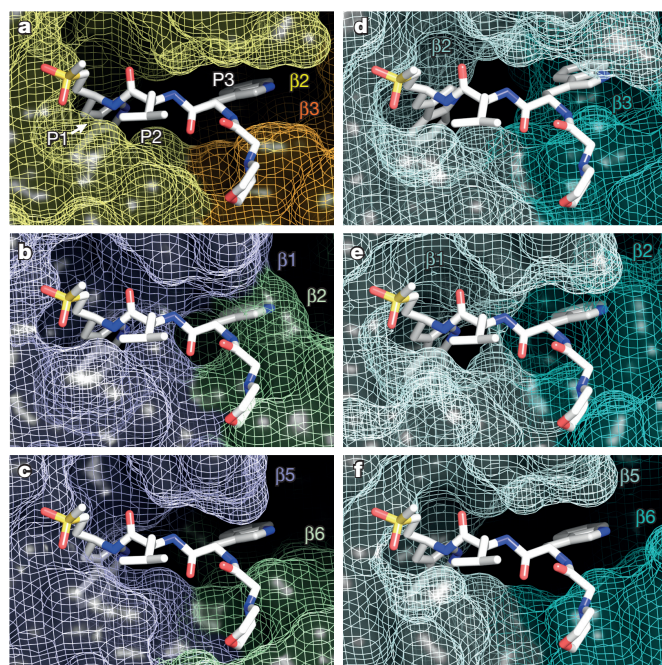


Figure 3 | Structural comparison of the *P. falciparum* and human proteasome 20S core active sites. **a**, Coordinates of the *P. falciparum* proteasome $\beta 2$ active site bound to WLW-vs. The inhibitor P1, P2 and P3 positions are indicated. **b**, **c**, Coordinates of the *P. falciparum* proteasome $\beta 1$ (**b**) and $\beta 5$ (**c**) active sites with superimposed coordinates of the WLW-vs inhibitor, as shown in **a**. **d–f**, Coordinates of the apo human proteasome 20S core (PDB 4R3O) $\beta 2$ (**d**), $\beta 1$ (**e**), and $\beta 5$ (**f**) active sites, with superimposed coordinates of the WLW-vs inhibitor, as shown in **a**. In all parts the protein is represented as van der Waals surfaces and the inhibitor as sticks.

Extended Data Fig. 4a). As parasites are normally insensitive to a pulse inhibition of the proteasome $\beta 2$ active site alone¹⁰, this emphasizes the heightened sensitivity of *P. falciparum* to proteasome inhibition in the presence of DHA.

We have previously shown that co-inhibition of the *Plasmodium* proteasome $\beta 2$ - and $\beta 5$ -subunits results in complete parasite growth attenuation at all stages of its blood cycle, even after short inhibitor treatment times¹⁰. WLL-vs is a potent inhibitor of the parasite $\beta 2$ and $\beta 5$ active sites, while only effective against the human $\beta 5$ activity (Figs 1g, 3 and Extended Data Fig. 1d, e). WLL-vs is therefore likely to have potent anti-malarial activity with minimal toxicity to the host, since a short inhibition of host $\beta 5$ activity is well tolerated in non-transformed mammalian cells²⁶. We treated live *P. falciparum* cultures and primary human fibroblasts for 1 h with WLL-vs, and were surprised to find that WLL-vs inhibited all three proteasome catalytic sites in *P. falciparum*, while having little effect on any of the human subunits until high micromolar concentrations (Fig. 4c). This increased potency is probably due to inhibitor accumulation in the intact parasites and enhanced inhibition of the parasite 26S proteasome (20S with regulatory subunit 19S proteasome complex)²⁷. This translated into a large therapeutic window for the WLL-vs inhibitor in 1 h and 72 h viability assays (Fig. 4d and Extended Data Fig. 1e). Although the *P. falciparum* proteasome inhibition corresponds well to the decrease in parasite survival (Fig. 4d), we sought to determine whether off-target toxicity was occurring. First, a diastereomer of WLL-vs containing a P1 D-Leu (WL(d)L-vs) showed a dramatic reduction in compound potency (Extended Data Fig. 5a–c), indicating that these compounds were not indiscriminately cytotoxic. Second, vinyl-sulfones can react with cysteine proteases²⁸; therefore, we assessed reactivity of WLL-vs towards *P. falciparum* cysteine proteases using the activity-based probe BODIPY-TMR-DCG04 (ref. 29). We observed inhibition of cysteine proteases with WLL-vs only at concentrations that were

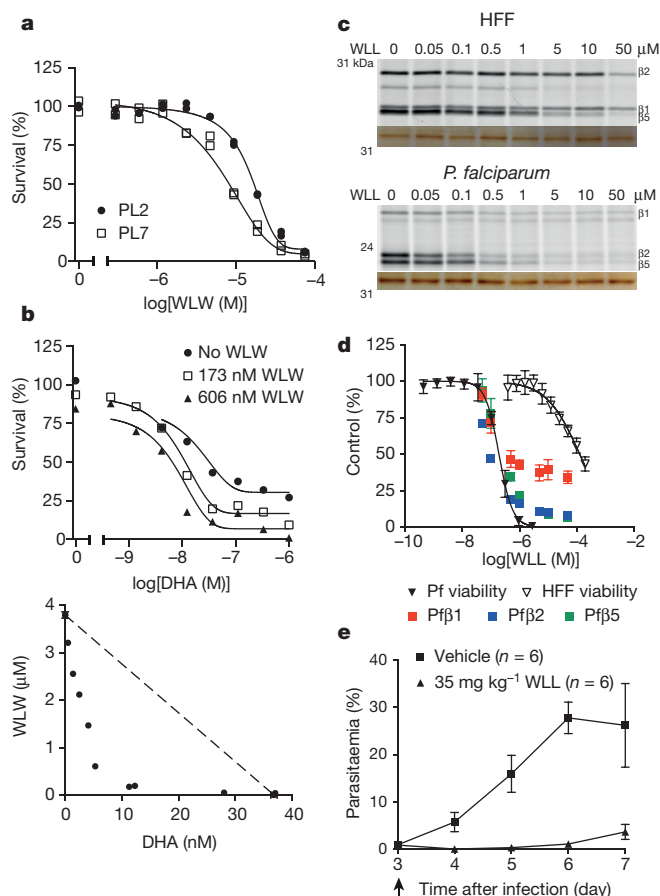


Figure 4 | Exploiting differences in the $\beta 2$ -subunits of the two proteasome species for selective parasite killing. **a**, **b**, $\beta 2$ -subunit-selective inhibitor WLL-vs can synergize with DHA treatment in ART-resistant *P. falciparum*. **a**, Viability 72 h after treatment for 1 h of ART-sensitive (PL2) and -resistant (PL7) parasites at early ring stage (2 h after invasion) with WLL-vs (abbreviated as WLW). **b**, Top, dose-response to DHA in the absence and presence of sublethal doses of WLW-vs. Bottom, isobologram of the two inhibitors at the 50% lethal dose. PL7 parasites were treated for 3 h at early ring stage (4 h after invasion). **a**, **b**, Data shown are individual data points (two technical replicates for **a**), representative of three independent experiments. **c–e**, WLL-vs co-inhibits $\beta 2$ along with the other two catalytic subunits, resulting in potent parasite killing. **c**, Human foreskin fibroblasts (HFFs) or *P. falciparum* schizonts were treated with WLL-vs for 1 h, and activity-based probe labelling was performed post-lysis (for gel source data, see Supplementary Fig. 1c, d). Fluorescent gel scan (top) and silver stain (bottom) are shown. **d**, Non-confluent, replicating HFFs ($n = 9$ cell cultures, from three independent experiments of triplicates) or *P. falciparum* at ring stage ($n = 6$ parasite cultures, from two independent experiments of triplicates) were pulse-treated for 1 h with WLL-vs and viability was determined after 71 h. Activities of the *P. falciparum* proteasome subunits after inhibitor treatment were determined as described in Methods ($n = 3$ parasite lysates from three independent experiments). Error bars, s.d. **e**, Balb/c female mice were infected with *P. chabaudi* and treated with a single intravenous dose of vehicle ($n = 6$ mice) or 35 mg kg⁻¹ WLL-vs ($n = 6$ mice) on day 3 after infection (arrow). Parasitaemia and weight of the mice were monitored daily until the infection was resolved naturally by the host (day 7 onwards). Error bars, s.d.

>tenfold over the 1 h treated half-maximum effective concentration (EC₅₀) (Extended Data Fig. 5d). Third, we assessed parasite morphology 24 h after a 1 h WLL-vs pulse treatment and observed arrested parasite development and eventual parasite death at high inhibitor concentrations (Extended Data Fig. 5e). The absence of a food vacuole defect indicated that the falcipains in this digestive organelle were not inhibited. Taken together, these data confirm that WLL-vs exerts its anti-malarial effects through direct proteasome inhibition.

Given the large therapeutic window of WLL-vs, we assessed its efficacy in a rodent *Plasmodium chabaudi* infection model. We infected Balb/c female mice with 1×10^6 parasites and treated them 3 days later using a single bolus dose of 35 mg kg⁻¹ WLL-vs or vehicle, by tail vein injection. We observed almost complete reduction of parasite burden after WLL-vs treatment (Fig. 4e) and good tolerance to the drug as assessed by appearance, activity, and weight retention (Extended Data Fig. 4b). The efficacy of this treatment was further confirmed in an intraperitoneal single bolus dosing study of mice infected with *P. chabaudi* (Extended Data Fig. 4c).

In summary, we have shown through biochemical and structural studies that the *Plasmodium* proteasome is sufficiently unique from the human proteasome for selective targeting. Furthermore we show that even sublethal doses of proteasome inhibitor can lead to parasite sensitization to ART. Our lead molecule, WLL-vs, is a mechanism-based peptidic inhibitor that is chemically similar to the US Food and Drug Administration-approved drug Kyprolis. We recognize that the unique disease epidemiology of malaria calls for stringent criteria in drug safety, stability, and delivery, and we are currently optimizing WLL-vs to generate a class of compounds with improved potency and oral bioavailability. Previous success in optimizing peptide-based agents³⁰ for efficient oral delivery offers promise in this class of inhibitors as next-generation anti-malarials.

Online Content Methods, along with any additional Extended Data display items and Source Data, are available in the online version of the paper; references unique to these sections appear only in the online paper.

Received 10 July; accepted 18 December 2015.

- Voges, D., Zwickl, P. & Baumeister, W. The 26S proteasome: a molecular machine designed for controlled proteolysis. *Annu. Rev. Biochem.* **68**, 1015–1068 (1999).
- Gantt, S. M. *et al.* Proteasome inhibitors block development of *Plasmodium* spp. *Antimicrob. Agents Chemother.* **42**, 2731–2738 (1998).
- Czesny, B., Goshu, S., Cook, J. L. & Williamson, K. C. The proteasome inhibitor epoxomicin has potent *Plasmodium falciparum* gametocytocidal activity. *Antimicrob. Agents Chemother.* **53**, 4080–4085 (2009).
- Kreidenweiss, A., Krensmeyer, P. G. & Mordmüller, B. Comprehensive study of proteasome inhibitors against *Plasmodium falciparum* laboratory strains and field isolates from Gabon. *Malar. J.* **7**, 187 (2008).
- Prudhomme, J. *et al.* Marine actinomycetes: a new source of compounds against the human malaria parasite. *PLoS ONE* **3**, e2335 (2008).
- Prasad, R. *et al.* Blocking *Plasmodium falciparum* development via dual inhibition of hemoglobin degradation and the ubiquitin proteasome system by MG132. *PLoS ONE* **8**, e73530 (2013).
- Mok, S. *et al.* Population transcriptomics of human malaria parasites reveals the mechanism of artemisinin resistance. *Science* **347**, 431–435 (2015).
- Mbengue, A. *et al.* A molecular mechanism of artemisinin resistance in *Plasmodium falciparum* malaria. *Nature* **520**, 683–687 (2015).
- Aminake, M. N., Arndt, H. D. & Pradel, G. The proteasome of malaria parasites: a multi-stage drug target for chemotherapeutic intervention? *Int. J. Parasitol.* **42**, 1–10 (2012).
- Li, H. *et al.* Assessing subunit dependency of the *Plasmodium* proteasome using small molecule inhibitors and active site probes. *ACS Chem. Biol.* **9**, 1869–1876 (2014).
- Li, H. *et al.* Validation of the proteasome as a therapeutic target in *Plasmodium* using an epoxylactone inhibitor with parasite-specific toxicity. *Chem. Biol.* **19**, 1535–1545 (2012).
- Stadtmueller, B. M. & Hill, C. P. Proteasome activators. *Mol. Cell* **41**, 8–19 (2011).
- Li, H. *et al.* Identification of potent and selective non-covalent inhibitors of the *Plasmodium falciparum* proteasome. *J. Am. Chem. Soc.* **136**, 13562–13565 (2014).
- O'Donoghue, A. J. *et al.* Destructin-1 is a collagen-degrading endopeptidase secreted by *Pseudogymnoascus destructans*, the causative agent of white-nose syndrome. *Proc. Natl Acad. Sci. USA* **112**, 7478–7483 (2015).
- O'Donoghue, A. J. *et al.* Global identification of peptidase specificity by multiplex substrate profiling. *Nature Methods* **9**, 1095–1100 (2012).
- Colaert, N., Helsens, K., Martens, L., Vandekerckhove, J. & Gevaert, K. Improved visualization of protein consensus sequences by iceLogo. *Nature Methods* **6**, 786–787 (2009).
- Harris, J. L., Alper, P. B., Li, J., Rechsteiner, M. & Backes, B. J. Substrate specificity of the human proteasome. *Chem. Biol.* **8**, 1131–1141 (2001).
- Kisselev, A. F., van der Linden, W. A. & Overkleeft, H. S. Proteasome inhibitors: an expanding army attacking a unique target. *Chem. Biol.* **19**, 99–115 (2012).
- Bogyo, M. *et al.* Covalent modification of the active site threonine of proteasomal β subunits and the *Escherichia coli* homolog HslV by a new class of inhibitors. *Proc. Natl Acad. Sci. USA* **94**, 6629–6634 (1997).
- da Fonseca, P. C. A. & Morris, E. P. Cryo-EM reveals the conformation of a substrate analogue in the human 20S proteasome core. *Nature Commun.* **6**, 7573–7576 (2015).
- Harshbarger, W., Miller, C., Diedrich, C. & Sacchettini, J. Crystal structure of the human 20S proteasome in complex with carfilzomib. *Structure* **23**, 418–424 (2015).
- Meshnick, S. R. Artemisinin: mechanisms of action, resistance and toxicity. *Int. J. Parasitol.* **32**, 1655–1660 (2002).
- Ashley, E. A. *et al.* Tracking Resistance to Artemisinin Collaboration (TRAC). Spread of artemisinin resistance in *Plasmodium falciparum* malaria. *N. Engl. J. Med.* **371**, 411–423 (2014).
- Stratimer, J. *et al.* Drug resistance. K13-propeller mutations confer artemisinin resistance in *Plasmodium falciparum* clinical isolates. *Science* **347**, 428–431 (2015).
- Dogovski, C. *et al.* Targeting the cell stress response of *Plasmodium falciparum* to overcome artemisinin resistance. *PLoS Biol.* **13**, e1002132 (2015).
- Britton, M. *et al.* Selective inhibitor of proteasome's caspase-like sites sensitizes cells to specific inhibition of chymotrypsin-like sites. *Chem. Biol.* **16**, 1278–1289 (2009).
- Bedford, L., Paine, S., Sheppard, P. W., Mayer, R. J. & Roelofs, J. Assembly, structure, and function of the 26S proteasome. *Trends Cell Biol.* **20**, 391–401 (2010).
- Palmer, J. T., Rasnick, D., Klaus, J. L. & Brömme, D. Vinyl sulfones as mechanism-based cysteine protease inhibitors. *J. Med. Chem.* **38**, 3193–3196 (1995).
- Arastu-Kapur, S. *et al.* Identification of proteases that regulate erythrocyte rupture by the malaria parasite *Plasmodium falciparum*. *Nature Chem. Biol.* **4**, 203–213 (2008).
- Zhou, H. J. *et al.* Design and synthesis of an orally bioavailable and selective peptide epoxylactone proteasome inhibitor (PR-047). *J. Med. Chem.* **52**, 3028–3038 (2009).

Supplementary Information is available in the online version of the paper.

Acknowledgements This work was supported by National Institutes of Health grants R01AI078947, R01EB05011 to M.B., and by the Medical Research Council grant MC-UP-1201/5 to P.C.A.d.F. H.L. was supported by an NNS-PhD scholarship from the Agency for Science, Technology and Research (A*STAR) Singapore. W.A.v.d.L. was supported by a Rubicon fellowship from the Netherlands Organization for Scientific Research (NWO). A.J.O. and C.S.C. were supported by the Program for Breakthrough Biomedical Research (PBBR) and the Sandler Foundation. I.T.F. was supported by American Heart Association grant 14POST20280004. We acknowledge support from the Australian Research Council and the Australian National Health and Medical Research Council. We thank K. Chotivanich for providing PL2 and PL7 parasites. We thank E. Yeh's group for help with *P. falciparum* D10 culture and for use of their equipment. We thank J. Boothroyd for providing the human fibroblast cells. We thank E. Morris and R. Henderson for discussions on image processing, FEI fellows and C. Sava for assisting in the use of the Titan Krios microscope, S. Chen for EM support, and J. Grimmet and T. Darling for computing support.

Author Contributions H.L., A.J.O., L.T., C.S.C., P.C.A.d.F. and M.B. designed the experiments and wrote the manuscript. H.L., W.L. and E.Y. performed chemical synthesis and analysis. H.L., S.C.X. and I.T.F. performed the inhibitor studies. P.C.A.d.F. did the electron microscopy and image analysis. All authors discussed the results and commented on the manuscript.

Author Information The cryo-EM map and the atomic coordinates of the inhibitor-bound *Plasmodium* 20S proteasome have been deposited in the Electron Microscopy Data Bank (EMDB) and PDB under accession numbers EMD-3231 and 5FMG, respectively. Reprints and permissions information is available at www.nature.com/reprints. The authors declare no competing financial interests. Readers are welcome to comment on the online version of the paper. Correspondence and requests for materials should be addressed to M.B. (mbogyo@stanford.edu) or P.C.A.d.F. (pauladf@mrc-lmb.cam.ac.uk).

METHODS

Materials for substrate profiling. Proteasome substrates Suc-LLVY-amc and human 20S proteasome were purchased from Boston Biochem. The *P. falciparum* 20S proteasome was purified as previously reported¹¹. The human PA28 α was a gift from Boston Biochem. The peptide library for substrate cleavage profiling was used as described in ref. 15.

Fluorogenic substrate assay. Substrate assays were performed in black 96-well Costar plates. For these assays, purified human or *P. falciparum* 20S proteasomes were activated using human PA28 α ¹³. Each enzyme was added to a final concentration of 1 nM and the reaction proceeded in the presence of 12.5 μ M Suc-LLVY-amc for 1 h at room temperature (21 °C). The slope over the linear range of the reaction was determined for each of the enzymes. All experiments were performed at least in triplicate.

Multiplex substrate profiling of human and *Plasmodium* proteasomes. The peptide library consisting of 228 tetradecapeptides was designed according to an algorithm previously reported¹⁵. Peptides were split into 2 pools of 114 for optimal liquid chromatography separation. *P. falciparum* and human 20S proteasomes were assayed at 2 nM, in the presence of 24 nM of PA28 α and 500 nM of each peptide. All assays were performed at room temperature in 20 mM HEPES, pH 7.5, and 0.5 mM EDTA. Aliquots were removed and acid quenched to pH 3.0 or less with formic acid (4% final) after incubation for 15, 60, and 240 min. A control sample lacking enzyme was also prepared under identical conditions to account for non-enzymatic degradation of the substrates. Each sample was de-salted with C18 tips (Rainin), and ~130 ng of total peptide was injected for mass spectrometry analysis. Peptide separation was performed using an EZ-Spray C18 column (Thermo, ES800, PepMap, 3 μ m bead size, 75 μ m \times 15 cm). Reverse-phase chromatography was performed at a flow rate of 600 nl min⁻¹ for loading and 300 nl min⁻¹ for using a nanoACQUITY (Waters) ultra-performance liquid chromatography instrument. A 60 min linear gradient from 2% to 30% acetonitrile in 0.1% formic acid was used, and mass spectrometry was performed on a LTQ Orbitrap XL. Survey scans were recorded over a 350–1500 *m/z* range, and peptide fragmentation was induced with collision-induced dissociation for tandem mass spectrometry. Collision-induced dissociation was performed on the six most intense precursor ions, with a minimum of 1,000 counts, using an isolation width of 2.0 atomic mass units, with 35% normalized collision energy. Data were analysed as previously reported using the in-house PAVA software to generate centroid peak lists, Protein Prospector software version 5.10.15 for data searches, and iceLogo software for visualization of amino-acid frequency surrounding the cleavage sites¹⁵. The Z-score was calculated using the standard formula and indicates deviation from the mean frequency of a specific amino acid on a specific position in a reference set of sequences.

***P. falciparum* replication assays.** *P. falciparum* D10 cultures were maintained, synchronized, and lysed as previously described¹¹. *P. falciparum* D10 was obtained originally from the Malaria Research and Reference Reagent Resource Center (MR4). Parasite cultures were grown in human erythrocytes (no blood type discrimination) purchased from the Stanford Blood Center (approved by Stanford University). Ring stage *P. falciparum* culture at 2% parasitaemia and 0.5% hematocrit was added to 96-well plates spotted with compounds. The *P. falciparum* culture was incubated with each compound for 1 h and 72 h. After compound treatment for 1 h, the inhibitor was removed and the culture was washed three times in media, before fresh media was added for a further 71 h of growth. After incubation, the culture was fixed in a final concentration of 1% paraformaldehyde (in PBS) for 30 min at room temperature. The nuclei stain YOYO-1 was then added to a final concentration of 50 nM and incubated overnight at 4 °C. Parasite replication was monitored by observation of a YOYO-1-positive population (infected) and YOYO-1-negative population (uninfected) using a BD Accuri C6 automated flow cytometer. Values in Extended Data Fig. 1e are the average \pm s.d.; *n* = 6 parasite cultures from two independent experiment of triplicates.

Cell viability assay in mammalian cells. HFFs used in all experiments were non-transformed primary cells (obtained from J. Boothroyd) derived from human foreskin tissues and tested for mycoplasma contamination. HFFs were plated at 2,500 cells (non-confluent) per well <24 h before addition of the compound. Compounds were diluted for dose–response concentrations in media, and added to the cells for 72 h. Cell viability was measured using the CellTiter-Blue Assay (Promega) as per the manufacturer's instructions. Values in Extended Data Fig. 1e are the average \pm s.d.; *n* = 9 cell cultures from three independent experiments of triplicates for HFF treatment, except for 1 h WLW-vs, 1 h LLW-vs, and 72 h LLL-vs, where *n* = 6 cell cultures from two independent experiment of triplicates.

Activity-based probe labelling of mammalian and *P. falciparum* proteasomes. BMV037 was used at a final concentration of 10 μ M to label *P. falciparum* proteasome activity, and MV151 was used at a final concentration of 2 μ M to label mammalian proteasome activity. Purified proteasomes (human or *P. falciparum*, 10 nM) were incubated with each inhibitor for 1 h at 37 °C before addition of

BMV037 or MV151 for a further 2 h at 37 °C. Samples were denatured by addition of SDS sample buffer, boiled briefly and run on a 12% SDS PAGE. Gels were scanned on the Cy5 channel (for BMV037) or the Cy3 channel (for MV151) on a Typhoon Scanner (GE Healthcare). Quantification of the intensity of the labelled proteins was done using Image J. A small amount of activation in the β 1-subunit was observed in the human proteasome after inhibitor treatment.

Assessment of *P. falciparum* proteasome activity in intact inhibitor treated parasites. *P. falciparum* was cultured to around 10% parasitaemia to ensure sufficient parasites were available for proteasome labelling. *P. falciparum* culture was first treated for the indicated amount of time, and spun down at 3,200 r.p.m (962g) to remove inhibitor. Each culture was then washed once in fresh media and *P. falciparum* lysate obtained as previously described¹¹. Proteasome labelling of the parasite lysate was performed as described above. To assess proteasome inhibition, the intensity of the proteasome labelling was quantified by Image J and the amount of proteasome inhibition was taken as a percentage of the dimethylsulfoxide (DMSO)-treated control.

Assessment of WLL-vs activity and DHA synergism against ART-sensitive and -resistant *P. falciparum*. Sensitivity of PL2 and PL7 *P. falciparum* strains (at 2 h after invasion) to a 1-h pulsed treatment with WLW-vs was determined as described previously²⁵. Interactions between DHA and WLW-vs against the K13 mutant strain, PL7, exposed to a 3-h pulsed treatment was determined at 4 h after invasion as described previously²⁵.

In vivo assessment of WLL-vs. All mouse experiments were approved by the Stanford Administration Panel on Laboratory Animal Care and strictly followed their specific guidelines. Sample size was determined on the basis of the minimum number of animals required for good data distribution and statistics. We ensured all animals in vehicle- and compound-treated groups had similar body weight before treatment. No inclusion or exclusion criteria were used as animals were randomly chosen for each group. No blinding was performed between the groups. For each drug assay, Balb/c female mice (~20 g, 6–8 weeks old) were infected by intraperitoneal injection with 1×10^6 *P. chabaudi* parasites isolated from an infected mouse on day 0. For the experiment presented in Fig. 4, the infected mice were dosed 3 days after infection with a single bolus tail vein injection either of vehicle (*n* = 6) comprising 10% DMSO, 10% (2-hydroxypropyl)- β -cyclodextrin in sterile PBS, or of WLL-vs (*n* = 6) formulated in the vehicle. For the experiment presented in Extended Data Fig. 4c, the infected mice were dosed 2 days after infection with a single bolus intraperitoneal injection either of vehicle (45% polyethylene glycol (relative molecular mass 400), 35% propylene glycol, 10% ethanol, 10% DMSO and 10% (w/v) 2-hydroxypropyl- β -cyclodextrin), or WLL-vs at 40 mg kg⁻¹, 60 mg kg⁻¹, and 80 mg kg⁻¹ body weight formulated in the vehicle. Both of the treatments were administered at night (21:00). Parasitaemia was monitored daily by Geimsa-stained thin blood smears obtained from the tail vein and quantified by light microscope counting, where a minimum of five fields, each containing at least 400 red blood cells, were counted. The health of the mice was also monitored daily by measuring their body weight and by assessment of their appearance and activity.

Assessment of *P. falciparum* cysteine protease activities. A mixed stage culture of red blood cells infected with *P. falciparum* D10 was treated with a range of concentrations of WLL-vs for 1 h at 37 °C. BODIPY-TMR-DCG04 (2 μ M) was then added to the culture for a further 1 h for live cell labelling of the activities of the parasitic cysteine proteases. JPM-OEt²⁹ (100 μ M) was added as a positive control. After probe labelling, the parasite pellet was isolated by saponin lysis and kept at –80 °C. For further analysis, the samples were thawed at 4 °C and lysed directly in sample buffer and loaded onto a 15% SDS–polyacrylamide gel electrophoresis. Fluorescence of the probe was detected using the Typhoon as described above.

Giemsa stain of WLL-vs treated *P. falciparum* culture. *P. falciparum* culture at mid-ring (9–12 h after invasion) was treated with DMSO or WLL-vs for 1 h at 37 °C and the inhibitor was removed. The culture was washed in media and left to grow in fresh media for a further 23 h. Culture was then spun down and the red blood cell pellet used to make a thin blood smear on glass slides, fixed with methanol and stained with Giemsa stain for light microscopy.

Chemical synthesis. The detailed procedures for chemical synthesis are presented in Supplementary Information.

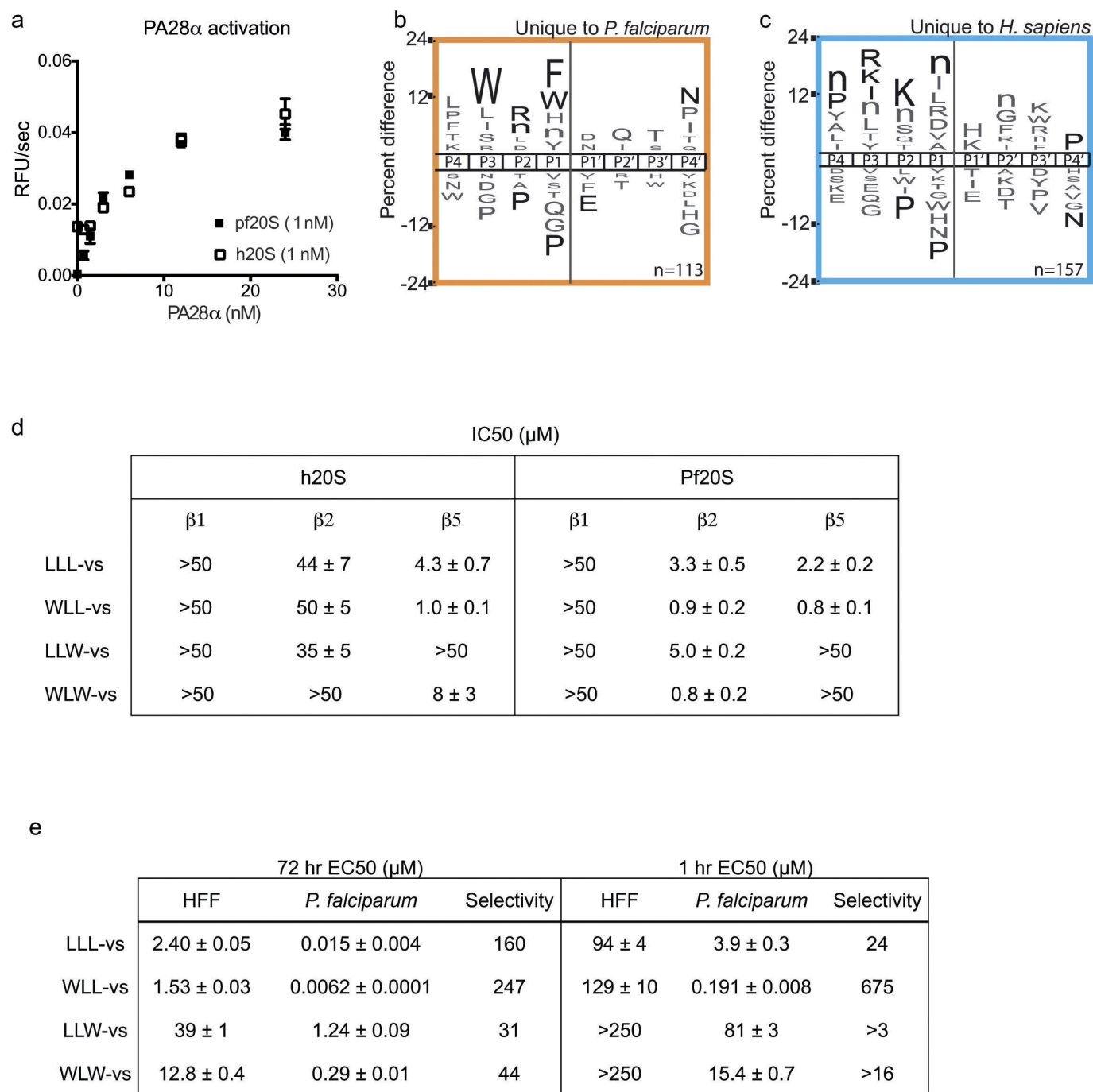
Cryo-EM data acquisition. A sample of *P. falciparum* 20S proteasome core was diluted in 50 mM Tris-HCl, pH 7.5, 5 mM MgCl₂, and 1 mM dithiothreitol, to a concentration of 0.14 μ M (0.1 mg ml⁻¹), and incubated in the presence of 10 μ M WLW-vs for 1 h at 37 °C. The sample was applied onto Quantifoil 1.2/1.3 electron microscope grids that were coated with a thin layer of carbon, freshly floated from mica, and glow-discharged in air. The grids were flash frozen by plunging into liquid ethane using a Vitrobot (FEI), operated at 22 °C and 95% humidity, with a 2.5 s blot time. The grids were transferred into a FEI Titan Krios microscope, operated at an acceleration voltage of 300 keV and a nominal magnification of \times 75,000 (yielding a calibrated sampling of 1.04 Å per pixel at the image level).

Images were recorded (from a single cryo-EM grid and during a single cryo-EM session) on a Falcon II direct electron detector, using EPU software, at a range of 1.70–3.16 μm underfocus and 1 s exposure time (Extended Data Fig. 3a). For each exposure 17 individual frames were captured at a rate of 0.056 s per frame, each corresponding to an electron dose of 2.8 electrons per square ångström. For each exposure, the image corresponding to the sum of all frames was used for screening for optimal ice thickness and image stability, as assessed by the isotropic recovery of Thon rings in their power spectra. From the 2,603 images recorded, 1,816 were selected for further processing.

Image processing. We used the same strategy for image analysis as for the recent determination of the structure of an inhibitor-bound human 20S proteasome core²⁰. For each exposure selected for image analysis, the sum of all frames captured was used to determine the defocus and astigmatism parameters, using the Tigris program findctf, and for particle selection, performed automatically in Relion³¹. This automated particle selection was carefully supervised with the manual removal of false positives and addition of false negatives. Further processing was performed using the sum of frames 3–10 of each exposure, effectively acquired within 0.45 s and corresponding to a total accumulated electron dose of 28 electrons per square ångström. This frame selection aimed at an adequate signal-to-noise ratio, for accurate determination of particle orientation, and the preservation of high-resolution information, as previously discussed²⁰. The phases of the resulting images were corrected for the contrast transfer function by phase flipping with the Tigris program flipctf, using the image defocus and astigmatism parameters determined as described above. Selected particle images were then extracted into 256 pixel \times 256 pixel boxes, resulting in a data set of 97,720 particles. The single-particle analysis refinement routine was performed using C2 symmetry and used the cryo-EM structure of the human 20S proteasome core (Electron Microscopy Data Bank accession code EMD-2981) as starting reference. This routine consisted of rounds of alignment and Euler angle assignment by projection matching, using the program AP SH of the Spider software package³², 3D reconstruction, using icr3d (which includes correction for the amplitude component of the contrast transfer function), and forward projection, using icr3dpro. The icr3d and icr3dpro programs are implemented in Tigris, a software package publicly available at <http://sourceforge.net>. A resolution limited approach was used to avoid noise over-fitting during refinement, where the 3D map obtained in each refinement cycle was carefully inspected, masked, and Fourier low-pass filtered to a conservative threshold in preparation of the reference for the next cycle. The surface representations of the final map as determined by the icr3d software (Fig. 2a, b), without further sharpening, Fourier filtering, or masking, were created using UCSF Chimera³³ and colour coded according to local resolution as determined by ResMap³⁴.

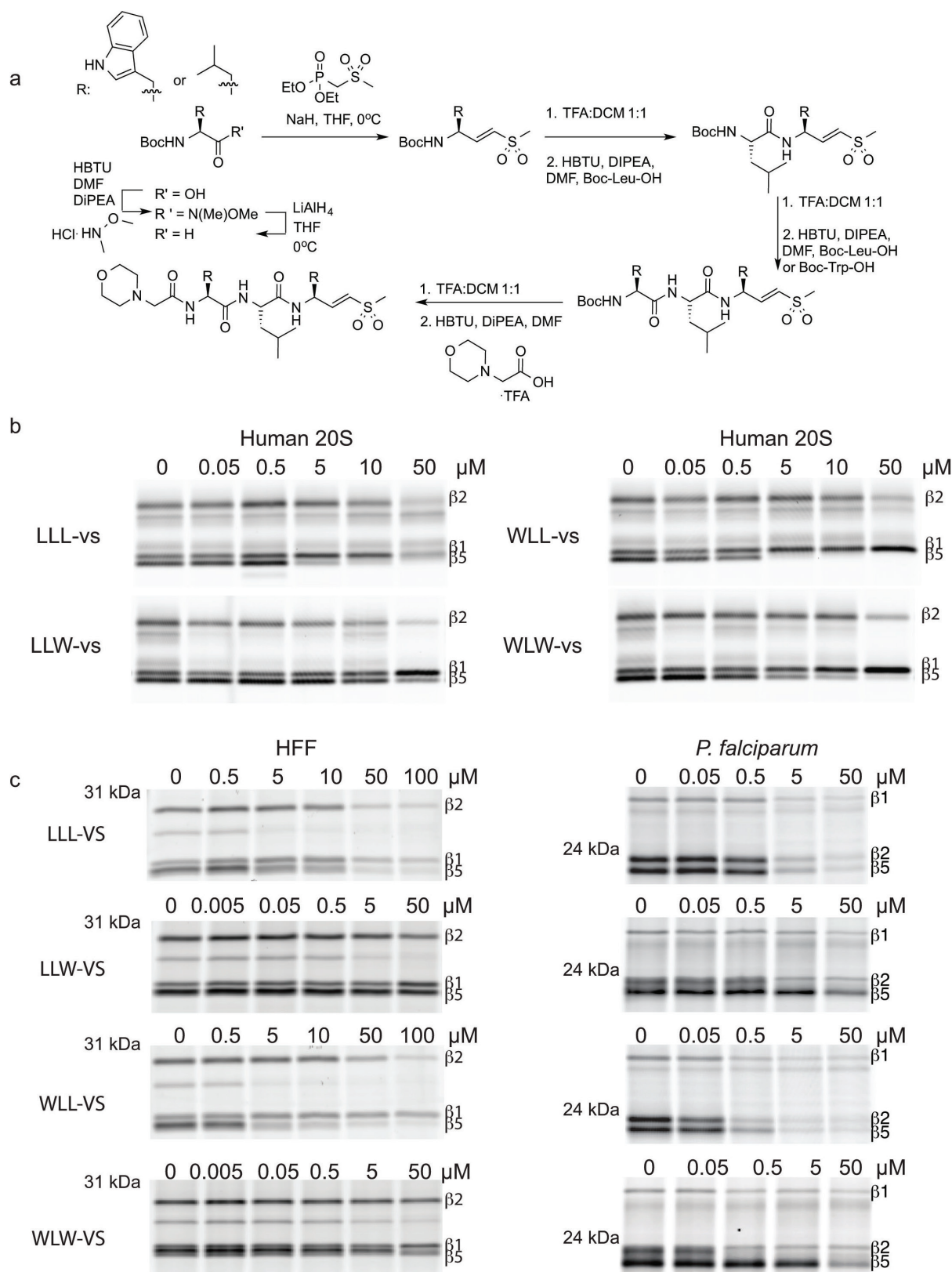
Molecular modelling. Molecular models for each of the *P. falciparum* proteasome 20S core subunits were originally obtained using the Phyre2 Protein Homology Recognition Engine³⁵, with the sequences deposited in the PlasmoDB (*Plasmodium* Genomics Resource). A preliminary fitting of these models was performed using molecular dynamics flexible fitting³⁶, which was followed by real-space refinement in Coot³⁷ and Phenix³⁸. Protein regions that were not well recovered in our map were not modelled. The final model was checked for geometry, close contacts, and bond parameters using MolProbity³⁹. The statistics obtained (Extended Data Fig. 3c) compared favourably with those for models determined by X-ray crystallography at similar resolutions, indicating that there was no over-fitting during model building. The resolution of the cryo-EM map can therefore be assessed by Fourier shell correlation against a density map generated from these coordinates, yielding a value of about 3.6 Å (Extended Data Fig. 3d). The mesh representations of the final map showing the fitted coordinates of the *P. falciparum* 20S proteasome core (Fig. 2c–g) were created using the PyMOL Molecular Graphics System. For these representations, the map was sharpened with a *B*-factor of –50 and Fourier low-pass filtered to 3.6 Å.

31. Scheres, S. H. W. Semi-automated selection of cryo-EM particles in RELION-1.3. *J. Struct. Biol.* **189**, 114–122 (2015).
32. Frank, J. et al. SPIDER and WEB: processing and visualization of images in 3D electron microscopy and related fields. *J. Struct. Biol.* **116**, 190–199 (1996).
33. Pettersen, E. F. et al. UCSF Chimera—a visualization system for exploratory research and analysis. *J. Comput. Chem.* **25**, 1605–1612 (2004).
34. Kucukelbir, A., Sigworth, F. J. & Tagare, H. D. Quantifying the local resolution of cryo-EM density maps. *Nature Methods* **11**, 63–65 (2014).
35. Kelley, L. A., Mezulis, S., Yates, C. M., Wass, M. N. & Sternberg, M. J. E. The Phyre2 web portal for protein modeling, prediction and analysis. *Nature Protocols* **10**, 845–858 (2015).
36. Trabuco, L. G., Villa, E., Mitra, K., Frank, J. & Schulten, K. Flexible fitting of atomic structures into electron microscopy maps using molecular dynamics. *Structure* **16**, 673–683 (2008).
37. Emsley, P., Lohkamp, B., Scott, W. G. & Cowtan, K. Features and development of Coot. *Acta Crystallogr. D* **66**, 486–501 (2010).
38. Afonine, P. V. et al. Towards automated crystallographic structure refinement with phenix.refine. *Acta Crystallogr. D* **68**, 352–367 (2012).
39. Chen, V. B. et al. MolProbity: all-atom structure validation for macromolecular crystallography. *Acta Crystallogr. D* **66**, 12–21 (2010).
40. Verdoes, M. et al. A fluorescent broad-spectrum proteasome inhibitor for labeling proteasomes in vitro and in vivo. *Chem. Biol.* **13**, 1217–1226 (2006).
41. Rosenthal, P. B. & Henderson, R. Optimal determination of particle orientation, absolute hand, and contrast loss in single-particle electron cryomicroscopy. *J. Mol. Biol.* **333**, 721–745 (2003).



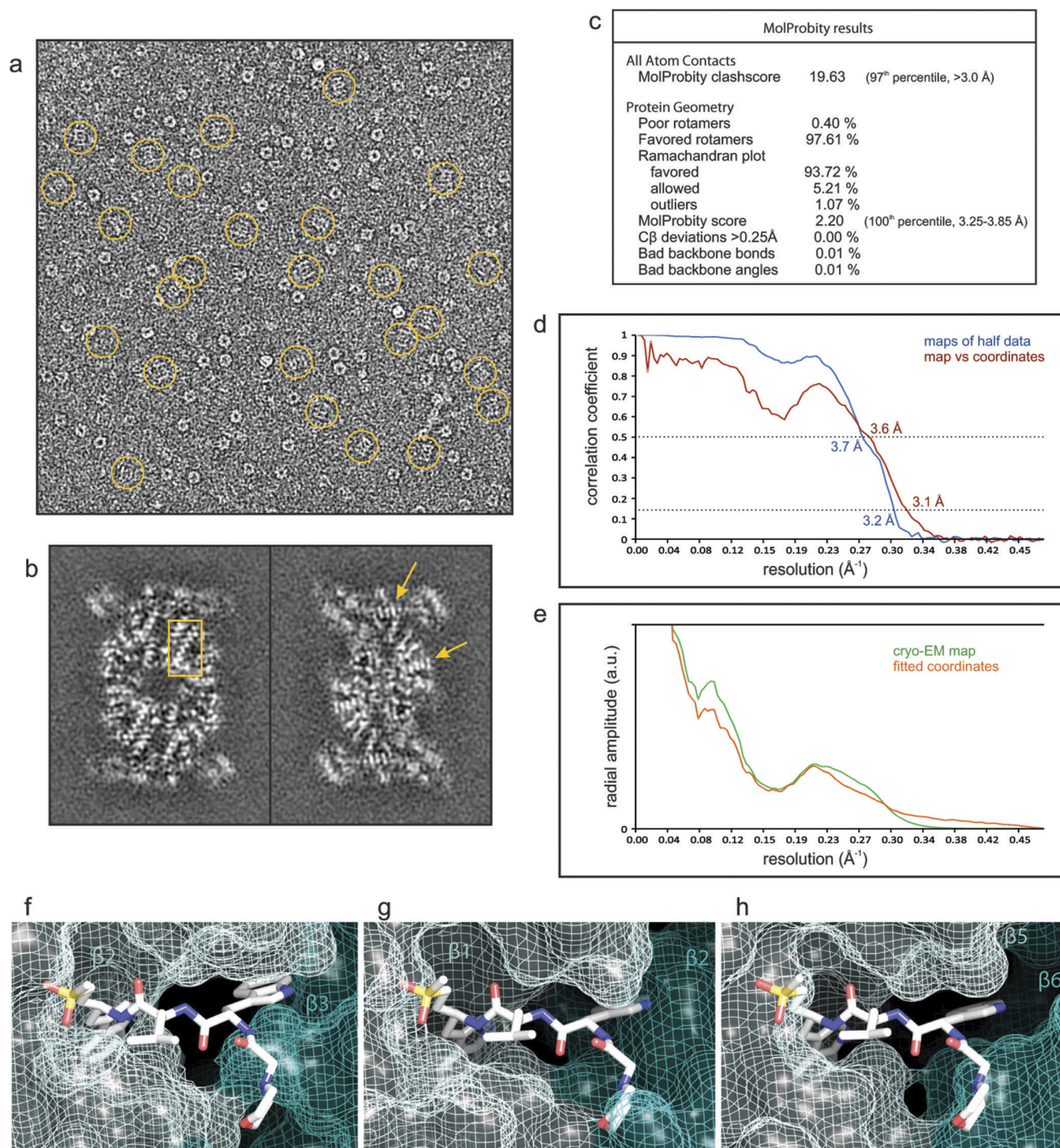
Extended Data Figure 1 | Activity, substrate specificity and inhibition of human and *P. falciparum* 20S proteasome. a–c, Substrate cleavage profile of activated human and *P. falciparum* 20S proteasome. a, Activation of the human and *P. falciparum* 20S proteasome by human PA28 α . Activity was determined by cleavage of the fluorogenic substrate Suc-LLVY-amc. Error bars, s.d. $n = 3$ purified proteasome in technical replicates. b, c, iceLogos of cleavage sequences that are uniquely processed either by the *P. falciparum* (b) or by the human proteasome (c). Amino acids that are most and least favoured at each position are shown above and below the axis, respectively. Lower-case 'n', norleucine; amino acids in black text are statistically significant ($P < 0.05$, unpaired two-tailed Student's t -test). d, e, Inhibition potencies of the vinyl sulfone inhibitors. d, Table of IC₅₀ values for each inhibitor in 1-h treated *P. falciparum* and human

20S proteasome. IC₅₀ values are determined from three independent experiments of inhibitor pretreatment followed by activity labelling of the 20S proteasome ($n = 3$ purified proteasome). Gels in Fig. 1f and Extended Data Fig. 2b were quantified to calculate the IC₅₀ values (for gel source data and replicates, see Supplementary Fig. 1a, b). Data are mean \pm s.d. e, Table of EC₅₀ values for each of the inhibitors in 1 h and 72 h treatment of *P. falciparum* at ring stage or non-confluent HFFs. Data are mean \pm s.d.; $n = 6$ parasite cultures from two independent experiment of triplicates for *P. falciparum* treatments; $n = 9$ cell cultures from three independent experiments of triplicates for HFF treatment, except for 1 h WLW-vs, 1 h LLW-vs, and 72 h LLL-vs, where $n = 6$ cell cultures from two independent experiments of triplicates.



Extended Data Figure 2 | Proteasome inhibitors preferentially inhibit $\beta 2$ of the *P. falciparum* proteasome. **a**, Vinyl sulfone inhibitors are synthesized from the Boc-protected amino acid by first generating the Weinreb amide, followed by the Horner–Wadsworth–Emmons reaction and standard peptide coupling. **b**, Purified human 20S proteasome was pre-treated for 1 h at 37 °C with each inhibitor followed by addition of activity-based probe MV151 (ref. 40) to assess for human proteasome

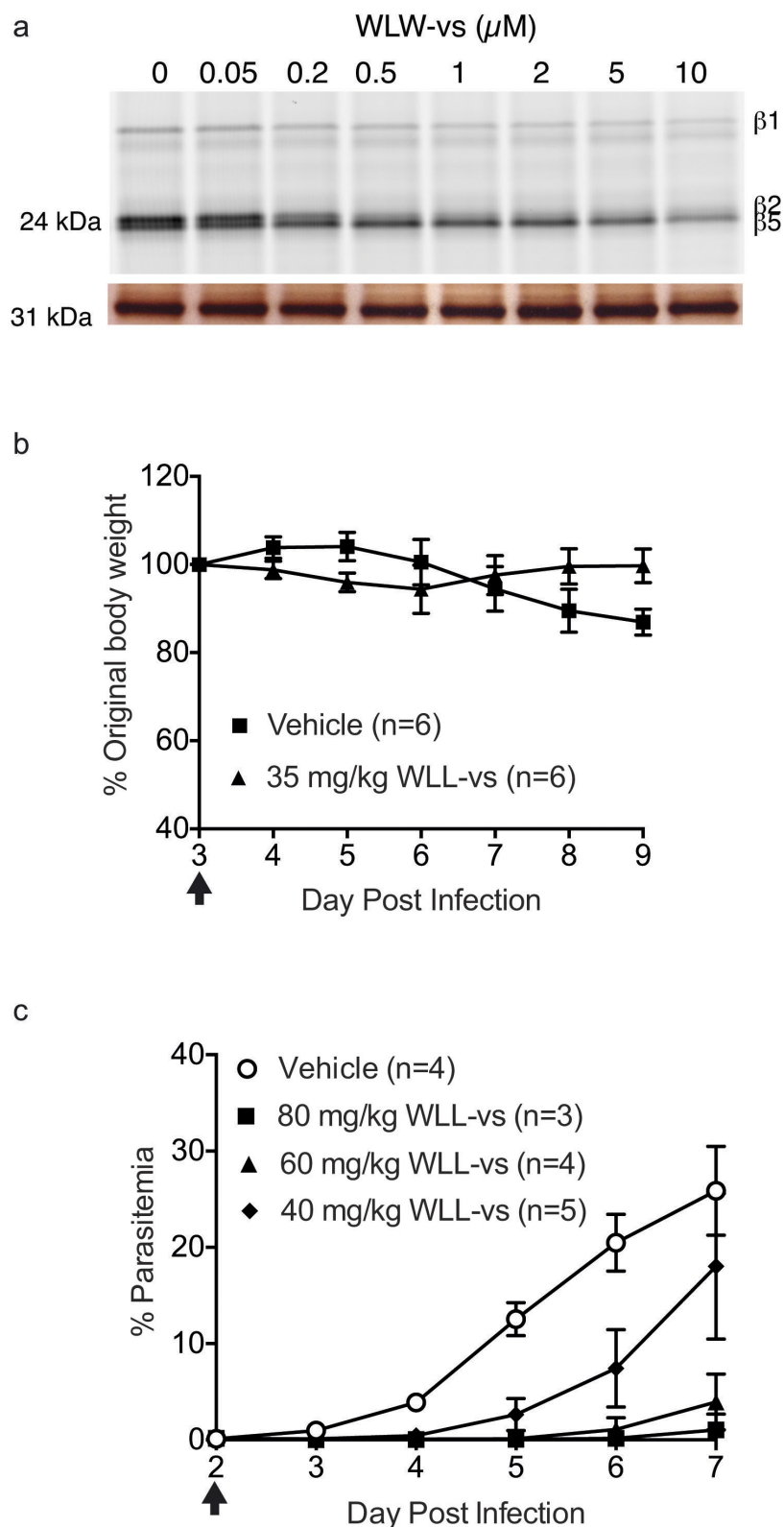
activities (for gel source data, see Supplementary Fig. 1b). **c**, HFF or *P. falciparum* culture was treated for 1 h at 37 °C with each inhibitor, followed by compound washout and post-lysis activity-based probe labelling. Gel shown for WLL-vs in *P. falciparum* is derived from Fig. 4c at the indicated concentrations to allow for direct comparison with other compounds (for gel source data, see Supplementary Fig. 1e).



Extended Data Figure 3 | Evaluation of the final cryo-EM map and molecular model of the *P. falciparum* 20S proteasome core.

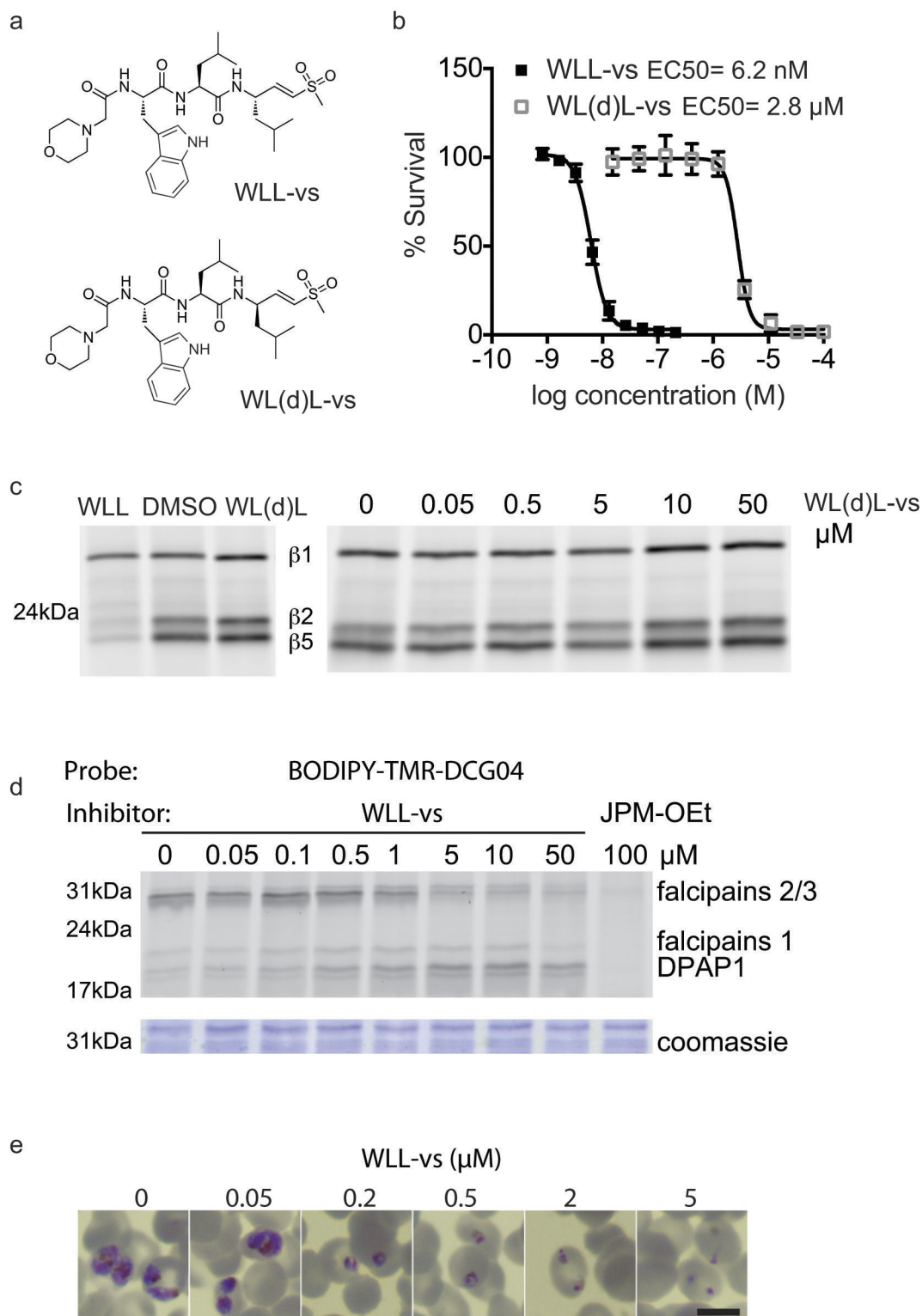
a–e, Evaluation of the single-particle analysis of the *P. falciparum* 20S proteasome core bound to the inhibitor WLW-vs. **a**, Cryo-EM image of the sample analysed, with molecular images of side views of the complex (normal to its long axis) indicated by rings. The image greyscale was inverted to show the protein densities in white. **b**, Individual sections of the 3D map, as determined by the 3D reconstruction algorithm (without further sharpening, masking, or Fourier filtering), are represented as grey scale. These sections are 1 Å thick and reveal the quality of the reconstruction, as the protein densities are clearly resolved against a very smooth background, with regions showing the pattern of α -helices (box) and the clear separation of sheet-forming β -strands (arrows) indicated. **c**, Evaluation of the model of the *P. falciparum* 20S proteasome core using MolProbity³⁹. **d**, Resolution estimate of the cryo-EM map by Fourier shell correlation. The curves correspond to the correlation obtained against the protein model (red) and the correlation between maps determined from

two halves of the data (blue). The resolution was estimated from the curve against the model where the 0.5 correlation coefficient criterion⁴¹ yields an estimate of 3.6 Å. The correlation coefficient can be seen to fall to a local minimum at ~6 Å and then recover at higher resolutions for both Fourier shell correlation curves. This behaviour is consistent with the rotationally averaged amplitude spectra of both the cryo-EM map and the coordinates (e). This region of the amplitude spectra contains reduced structural information, typical of protein scattering, indicating that these effects in the Fourier shell correlation curves arise from a genuine local reduction in the signal:noise ratio. **f–h**, Accessibility of the human 20S proteasome active sites to the inhibitor WLW-vs, using the protein model of the human proteasome core complex bound to an LLL-vs inhibitor²⁰. Protein coordinates of the human proteasome 20S core (PDB 5A0Q) β 2 (**f**), β 1 (**g**), and β 5 (**h**) active sites were aligned to the coordinates of the *P. falciparum* proteasome β 2-subunit bound to the WLW-vs inhibitor. The model of the human 20S proteasome active sites is represented as van der Waals surfaces with the superimposed WLW-vs inhibitor shown as sticks.



Extended Data Figure 4 | Intact cell treatment and *in vivo* treatment of vinyl sulfone inhibitors. **a**, WLW-vs was incubated in early trophozoite *P. falciparum* culture for 3 h, washed out, and the parasite lysate was incubated with probe BMV037. Top gel, the fluorescent scan; bottom gel, the silver stain. For gel source data, see Supplementary Fig. 1f. **b**, Body weight of WLL-vs- and vehicle-treated Balb/c mice after compound treatment by tail vein injection (Fig. 4e), expressed as a percentage of the original body weight on day 3 before compound treatment. Body weight of vehicle-treated mice decreased after day 6 of infection as part of the response to the natural resolution of the *P. chabaudi* infection. Treatment

day is indicated by arrow; $n = 6$ mice for each group; error bars, s.d. **c**, Balb/c female mice infected with 1×10^6 *P. chabaudi* parasites from passage host on day 0 were treated with a single bolus dose of vehicle (45% polyethylene glycol (relative molecular mass 400), 35% propylene glycol, 10% ethanol, 10% DMSO, and 10% (w/v) 2-hydroxypropyl- β -cyclodextrin; $n = 4$ mice) or WLL-vs at 40 mg kg^{-1} ($n = 5$ mice), 60 mg kg^{-1} ($n = 4$ mice), and 80 mg kg^{-1} ($n = 3$ mice) formulated in the vehicle. Treatment was performed on day 2 after infection as indicated by the arrow and administered by intraperitoneal injection. Parasitaemia was monitored daily by Giemsa stain of thin blood smears. Error bars, s.d.



Extended Data Figure 5 | Assessing off-target activities of WLL-vs.

a, Structures of WLL-vs and its diastereomer WL(d)L-vs. **b**, Dose-response curves of WLL-vs and WL(d)L-vs after 72 h treatment in *P. falciparum*. Error bars, s.d. ($n = 6$ parasite cultures for WLL-vs from triplicates of two independent experiments, and $n = 8$ parasite cultures for WL(d)L-vs over three independent experiments). **c**, Purified *P. falciparum* 20S proteasome was treated for 1 h at 37 °C with 10 μM of WLL-vs and WL(d)L-vs (left) or a range of concentrations of WL(d)L-vs. Residual activity was assessed by probe BMV037 (for gel source data, see Supplementary Fig. 1g).

d, A mixed-stage culture of *P. falciparum* was treated for 1 h with WLL-vs at 37 °C, followed by BODIPY-TMR-DCG04 for a further 1 h. Samples were directly loaded onto SDS-polyacrylamide gel electrophoresis for analysis. JPM-OEt (100 μM) was included as positive control. The fluorescent scan is shown at the top and the Coomassie stain is shown at the bottom. For gel source data, see Supplementary Fig. 1h. **e**, Geimsa stain of 1 h treated *P. falciparum* ring 24 h after inhibitor was added. Scale bar, 600 μm.